

Effects of Halo Spin on the Formation and Evolution of Bars in Disk Galaxies

DAJEONG JANG¹ AND WOONG-TAE KIM^{1,2}

¹*Department of Physics & Astronomy, Seoul National University, Seoul 08826, Republic of Korea*

²*SNU Astronomy Research Center, Seoul National University, Seoul 08826, Republic of Korea*

ABSTRACT

The spin of dark halos has been shown to significantly affect bar formation and evolution in disk galaxies. To understand the physical role of the halo spin on bar formation, we run N -body simulations of isolated, Milky Way-sized galaxies by varying the halo spin parameter in the range $-0.16 \leq \lambda \leq 0.16$ and the bulge mass. We find that our adopted halo *alone* is subject to swing amplification of an $m = 2$ non-axisymmetric mode rotating in the same sense as the halo, which assists or inhibits the bar formation in a disk depending on its sense of rotation. The $m = 2$ mode in the disk, growing via swing amplification, interacts constructively (destructively) with the $m = 2$ mode in the prograde (retrograde) halo, promoting (delaying) bar formation. A bar grows by losing its angular momentum primarily to a halo. Since the halo particles inside (outside) the corotation resonance with the bar can emit (absorb) angular momentum to (from) the bar, the bar pattern speed decays slower for larger $\lambda > 0$, while it decreases relatively fast almost independent of $\lambda \leq 0$. Models with a strong bar develop a boxy peanut-shaped bulge. In models without a bulge, this occurs rapidly via buckling instability, while the bars with a bulge thicken gradually without undergoing buckling instability. Among the models considered in the present work, the bar in the $\lambda = 0.06$ model with a bulge of 10% of the disk mass best describes the Milky Way in terms of the bar length and pattern speed.

Keywords: Disk Galaxies (391), Milky Way Galaxy (1054), Galaxy dark matter halos (1880), Galaxy Bulges (578), Galaxy Disks (589), Barred Spiral Galaxies (136), Galaxy Bars (2364)

1. INTRODUCTION

Nearly 2/3 of disk galaxies in the local universe possess a weak or strong bar in optical and near-infrared images (de Vaucouleurs 1963; Whyte et al. 2002; Laurikainen et al. 2004; Marinova & Jogee 2007; Menéndez-Delmestre et al. 2007; Aguerri et al. 2009; Méndez-Abreu et al. 2012; Buta et al. 2015; Díaz-García et al. 2016, 2019). Bars are one of the main drivers of the dynamical and secular evolution of disk galaxies, responsible for stellar migration (Di Matteo et al. 2013; Kawata et al. 2017; Halle et al. 2018; Iles et al. 2024), angular momentum transport from disk to halo (Saha & Naab 2013; Petersen et al. 2016; Collier et al. 2018; Collier & Madigan 2021), and formation of pseudo bulges (Combes & Sanders 1981; Combes et al. 1990; Athanassoula 2005; Debattista et al. 2006; Gadotti 2011). Despite the im-

portance of bars, however, there has been no clear answer as to why some galaxies are barred or non-barred and what controls the physical properties of bars.

Many numerical studies have attempted to find one-parameter conditions for bar formation using the initial galaxy properties such as the ratio of the kinetic to gravitational potential energy and the ratio of the bulge to disk mean density (Ostriker & Peebles 1973; Efstathiou et al. 1982; Kataria & Das 2018; Saha & Elmegreen 2018). While the proposed conditions explain the bar formation in their own adopted models, they fail to be applicable to diverse galaxy models. The most likely reasons for this may be that the proposed conditions are based on a limited set of galaxy models by fixing either bulge or halo parameters and that the one-parameter conditions cannot capture the complicated processes of bar formation. Recently, Jang & Kim (2023, hereafter JK23) proposed the two-parameter condition

$$\left(\frac{Q_{T,\min}}{1.2}\right)^2 + \left(\frac{\text{CMC}}{0.05}\right)^2 \lesssim 1 \quad (1)$$

for bar formation. In Equation (1), $Q_{T,\min}$ is the minimum value of the Toomre stability parameter of the disk and CMC denotes the central mass concentration. This condition is physically motivated: bar formation requires several cycles of swing amplification and feedback loops (Sellwood 1980; Toomre 1981; Binney & Tremaine 2008), and perturbations grow more easily in a disk with smaller $Q_{T,\min}$ and CMC. Equation (1) implies that the presence of a (massive) halo tends to suppress bar formation by increasing both $Q_{T,\min}$ and CMC, which is qualitatively consistent with the established result that the density of a halo has a negative influence on the bar formation (Ostriker & Peebles 1973; Hohl 1976; Efstathiou et al. 1982; Debattista & Sellwood 2000).

While Equation (1) accounts for bar formation in diverse galaxy models with various degrees of the central concentration of halo and bulge, it is limited to models with a non-rotating halo. Cosmological simulations of galaxy formation found that dark halos acquire angular momentum from tidal torque (e.g., Hoyle 1951; Fall & Efstathiou 1980; White 1984) and satellite accretion (e.g., Vitvitska et al. 2002; Dillamore et al. 2023). As a dimensionless measure of halo spin, Bullock et al. (2001) introduced

$$\lambda \equiv \frac{L_{\text{vir}}}{\sqrt{2}M_{\text{vir}}r_{\text{vir}}V_c}, \quad (2)$$

where L_{vir} and M_{vir} are the angular momentum and mass within the virial radius r_{vir} , respectively, and $V_c = (GM_{\text{vir}}/r_{\text{vir}})^{1/2}$ is the circular velocity at r_{vir} .¹ Note that positive (negative) λ corresponds to a spinning halo in the same (opposite) sense as the disk rotation. Cosmological simulations showed that λ follows a lognormal distribution, with the mean value $\lambda \simeq 0.03$ – 0.04 (Bullock et al. 2001; Hetzner & Burkert 2006; Bett et al. 2007; Jiang et al. 2019). The Milky Way halo is also thought to spin with $\lambda = 0.061$ (Obreja et al. 2022).

N -body simulations for bar formation with a spinning halo commonly found that a stellar disk embedded in a prograde halo with larger λ (> 0) develops a bar faster (Saha & Naab 2013; Long et al. 2014; Collier et al. 2018; Collier & Madigan 2021; Kataria & Shen 2022; Li et al. 2024), while bar formation in a disk under a retrograde halo with smaller λ (< 0) is progressively delayed (Collier et al. 2019a). To explain this, Saha & Naab (2013) invoked the condition $t_{\text{OP}} \equiv T_{\text{rot}}/|W| > 0.14$ of Os-

triker & Peebles (1973) for bar formation, where T_{rot} and W refer to the rotational and gravitational potential energies of a galaxy, respectively. They argued that the halo spin increases T_{rot} to form a bar faster. Since Ostriker & Peebles (1973) employed models with a non-rotating, fixed halo, however, it is questionable whether T_{rot} should include the disk rotation only or the halo rotation as well. Even if the halo rotation can be included, t_{OP} is independent of the sense of halo rotation, as Saha & Naab (2013) noticed, which is not compatible with the numerical results: a bar forms earlier in a model with λ (> 0) than in the $-\lambda$ counterpart. This makes t_{OP} inadequate for explaining the effect of the halo spin on bar formation.

Once a bar forms, the angular momentum transfer between it and its surrounding halo affects the bar growth significantly. When $\lambda = 0$, a bar grows by losing its angular momentum to a halo (Athanasoula 2002; Martinez-Valpuesta et al. 2006; Kataria & Das 2018; Saha & Elmegreen 2018; JK23). The angular momentum transfer appears more complicated when the halo spin is considered. Long et al. (2014) found that the inner part of a prograde halo loses its angular momentum to a bar, while the outer part acquires it. Collier et al. (2019b) suggested that the angular momentum transfer by the resonances is more active under a halo with higher $\lambda > 0$. Collier et al. (2019a) and Collier & Madigan (2021) proposed that orbital reversals of halo particles are a crucial factor of angular momentum transfer between disk and halo with $\lambda < 0$. Kataria & Shen (2022) found that it is the spin of the inner halo (with $R < 30$ kpc) rather than the total halo spin that is important for the bar formation and its ensuing evolution.

In this paper, we use N -body simulations to investigate the effects of halo spin and the presence of a classical bulge on the bar formation and evolution. Our primary purpose is to understand how the halo spin physically affects the bar formation. For this, we consider Milky Way-sized galaxy models with differing bulge mass and halo spin. To delineate the effect of halo spin, we consider a wide range of the spin parameter $-0.16 \leq \lambda \leq 0.16$, and compare the results from halo-only models with $\lambda = \pm 0.16$ or 0. We monitor the temporal changes of the bar strength and pattern speed, study the vertical buckling of bars in our simulations, and analyze their dependencies on the spin parameter.

This paper is structured as follows. In Section 2, we describe our galaxy models and numerical methods. In Section 3, we run simulations without a disk and bulge to study the gravitational susceptibility of our adopted halos. In Section 4, we present the results of full galaxy models, focusing on the dependence on λ of the bar for-

¹ Equation (2) was derived from $\lambda_P = L|E|^{1/2}/(GM^{5/2})$, where L , E , and M refer to the total angular momentum, energy, and mass of a spherical system within radius r , respectively (Peebles 1969, 1971; see also Ansar & Das 2023). At the virial radius where $E = -GM_{\text{vir}}/(2r_{\text{vir}})$, λ in Equation (2) becomes identical to λ_P .

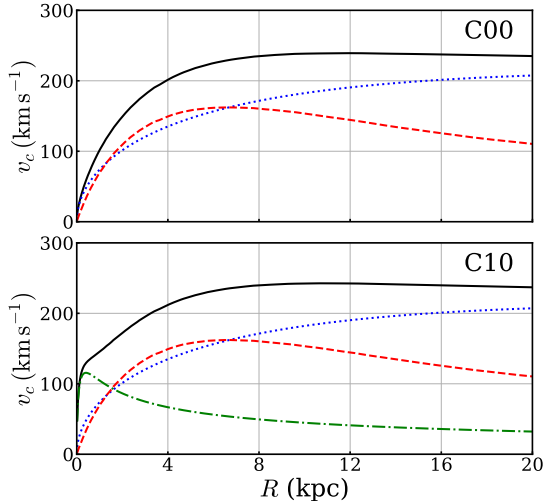


Figure 1. Radial distributions of the total circular velocity v_c (black solid) as well as the contributions of a halo (blue dotted), a disk (red dashed), and a bulge (green dot-dashed). The C00 and C10 series in the upper and lower panels refer to the models without and with a classical bulge, respectively.

mation, evolution, pattern speed, and angular momentum transfer. We also present the results for vertical buckling instability of our models and its outcomes. In Section 5, we discuss our results in comparison with the previous results and constrain the model parameters for the Milky Way. Finally, we conclude our work in Section 6.

2. GALAXY MODEL AND METHOD

To study the effects of halo spin on bar formation and evolution, we consider isolated galaxy models whose mass and size are similar to those of the Milky Way. Our galaxy models consist of a dark matter halo, a stellar disk, and a central supermassive black hole. Some models do not have a classical bulge (C00 series), but we also consider models with a bulge (C10 series).

The stellar disk has the conventional exponential-secant hyperbolic density distribution

$$\rho_d(R, z) = \frac{M_d}{4\pi z_d R_d^2} \exp\left(-\frac{R}{R_d}\right) \operatorname{sech}^2\left(\frac{z}{z_d}\right), \quad (3)$$

where R is the cylindrical radius, z is the vertical height, R_d is the disk scale radius, z_d is the disk scale height, and M_d is the total disk mass. We take $R_d = 3$ kpc, $z_d = 0.3$ kpc, and $M_d = 5 \times 10^{10} M_\odot$, similar to the Milky Way (Bland-Hawthorn & Gerhard 2016, Helmi 2020).

Both the halo and classical bulge have a density distribution that follows Hernquist (1990) profile

$$\rho(r) = \frac{M}{2\pi} \frac{a}{r(r+a)^3}, \quad (4)$$

Table 1. Model parameters

Name	M_b/M_d	λ	f_p
C00P16	...	0.16	1.00
C00P10	...	0.10	0.80
C00P06	...	0.06	0.67
C00P00	...	0.00	0.50
C00R06	...	-0.06	0.32
C00R10	...	-0.10	0.20
C00R16	...	-0.16	0.00
C10P16	0.1	0.16	1.00
C10P10	0.1	0.10	0.80
C10P06	0.1	0.06	0.67
C10P00	0.1	0.00	0.50
C10R06	0.1	-0.06	0.32
C10R10	0.1	-0.10	0.20
C10R16	0.1	-0.16	0.00

where $r = (R^2 + z^2)^{1/2}$ is the spherical radius, and M and a indicate the mass and the scale radius of each component, respectively. For the halo, we fix its mass and scale radius to $M_h = 1.3 \times 10^{12} M_\odot = 26M_d$ and $a_h = 30$ kpc, similar to the Milky Way (e.g., Bland-Hawthorn & Gerhard 2016, Helmi 2020). For the bulge, we set its scale radius to $a_b = 0.4$ kpc and mass to $M_b = 0.1M_d$ (e.g., Shen et al. 2010, Bland-Hawthorn & Gerhard 2016, Helmi 2020). We place a supermassive black hole with mass $M_{\text{BH}} = 4 \times 10^6 M_\odot$ at the galaxy center (Ghez et al. 2008; Gillessen et al. 2009a,b). Figure 1 plots the total circular velocity v_c calculated from the gravitational potential and the contribution of each component for the models in the C00 and C10 series. Due to the bulge, v_c in the C10 series increases rapidly at small R compared to that in the C00 series.

To assign the spin parameter λ to the dark halo, we follow the method of Long et al. (2014) and Collier et al. (2018, 2019a). That is, we randomly select a fraction of the halo particles and change the directions of their tangential velocities, while keeping their amplitudes and radial velocities intact. While Kataria & Shen (2022) explored the models in which the fraction f_p of the halo particles on prograde orbits with respect to the disk rotation varies with radius, we keep f_p spatially constant for simplicity. It turns out that our halo has $\lambda = 0.16$ when $f_p = 1$. The prograde fraction f_p decreases as λ decreases, leading to $\lambda = 0$ for $f_p = 0.5$, and $\lambda = -0.16$ for $f_p = 0$. This simple method of the velocity reversals does not change the Boltzmann equation and thus makes the density profile of the halo unchanged by vary-

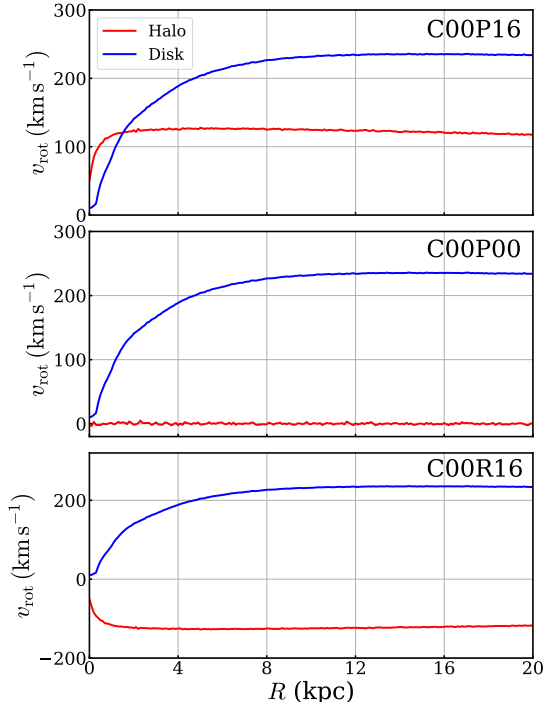


Figure 2. Radial distributions of the halo and disk rotational velocity v_{rot} for C00P16, C00P00, and C00R16.

ing λ (Lynden-Bell 1960; Weinberg 1985; Long et al. 2014; Collier et al. 2018, 2019b). In our halo model, the maximum and minimum value of λ is ± 0.16 , corresponding to either all prograde or all retrograde particles.

Table 1 lists the names, bulge-to-disk mass ratio, spin parameter λ , and prograde fraction f_p of our models. The models in the C00 series do not possess a bulge, while those in the C10 series have a bulge whose mass is 10% of the disk mass. The infixes P and R stand for a prograde and retrograde halo, respectively, and the numbers after the infixes denote λ multiplied by 100. Note that the models C00P00 and C10P00 have a non-spinning halo, and are identical to models C00 and C10 presented in JK23, respectively. In the present work, we do not consider the rotation of a bulge: the effect of bulge rotation was recently studied by Li et al. (2024).

Figure 2 compares the rotational velocities $v_{\text{rot}} = \langle v_\phi \rangle$ for the disk and halo in models C00P16, C00P00, and C00R16. Here, v_ϕ is the azimuthal velocities of the particles and the angle brackets denote the azimuthal and vertical averages. Note that v_{rot} is slightly smaller than v_c shown in Figure 1, corresponding to asymmetric drift (e.g., Oh et al. 2008). In model C00P00, the rotational velocity of the halo is nearly zero. However, when all halo particles move in the same azimuthal direction, the rotational velocity of the halo particles is almost flat, amounting to $v_{\text{rot}} \sim \pm 120 \text{ km s}^{-1}$ at $R \gtrsim 1 \text{ kpc}$. We

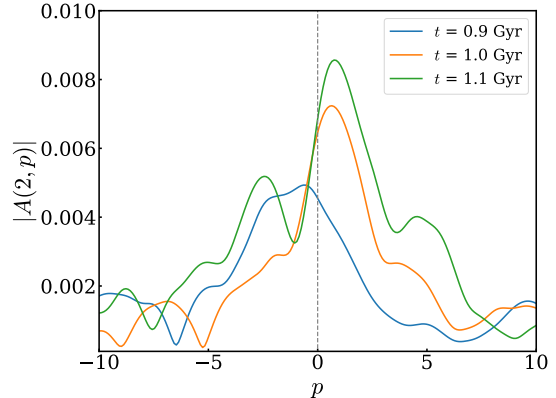


Figure 3. Evolution of the Fourier coefficients with dimensionless wavenumber p , defined in Equation (5), of the $m = 2$ logarithmic arms in the regions with $R \leq 5 \text{ kpc}$ and $|z| \leq 5 \text{ kpc}$ of the halo-only model with $\lambda = 0.16$. The dominant mode at $t = 0.9, 1.0, 1.1 \text{ Gyr}$ has $p = -0.6, 0.6, 0.8$, respectively.

will show in Section 3 that the halo rotation and velocity shear results in the creation of spirals, evolving into a weak bar, via swing amplification of density perturbations even in a halo-only system with $\lambda = \pm 0.16$.

To construct our galaxy models, we utilize the GALIC code (Yurin & Springel 2014) which finds a desired equilibrium by adjusting the velocities of individual particles to the level that satisfies the collisionless Boltzmann equations. The number of particles used is $N_d = 1.0 \times 10^6$, $N_b = 1.0 \times 10^5$, and $N_h = 2.6 \times 10^7$ for the disk, bulge, and halo, respectively. The mass of a single particle is set to $\mu = 5 \times 10^4 M_\odot$, which is equal for all three components.

We evolve our galaxy models until $t = 10 \text{ Gyr}$ using a public version of the Gadget-4 code (Springel et al. 2021). We take the multipole expansion of order $p = 4$ for fast force evaluation and a hierarchical time-integration scheme to reduce the computation time. We fix the force accuracy parameter to $\alpha = 3 \times 10^{-4}$ and the softening parameter to 0.05 kpc, 0.01 kpc, and 0.01 kpc for the halo, disk, and bulge particles, respectively, which we check conserves the total angular momentum within $\sim 0.1\%$.

3. HALO-ONLY MODELS

A rotating halo may be prone to forming weak, non-asymmetric structures via swing amplification, just as in a rotating disk. To explore this possibility, we run N -body simulations of halo-only models with $\lambda = 0.0$ (no spin), 0.16 (prograde), and -0.16 (retrograde), constructed in Section 2. By evolving these isolated halo models up to $t = 2 \text{ Gyr}$, we confirm that the azimuthally-averaged, radial distributions of halo den-

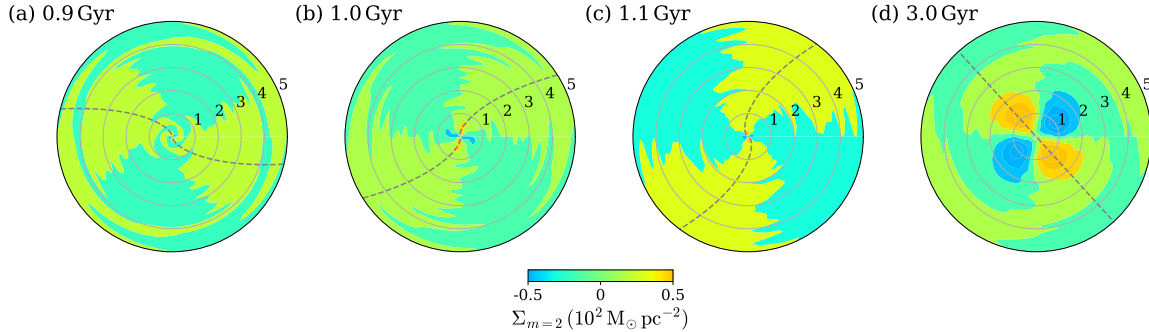


Figure 4. Projected density distributions of the $m = 2$ mode in the regions with $|z| \leq 5$ kpc and $R \leq 5$ kpc for the halo-only model with $\lambda = 0.16$ at (a) $t = 0.9$ Gyr, (b) $t = 1.0$ Gyr, (c) $t = 1.1$ Gyr, and (d) $t = 3.0$ Gyr. In each panel, the concentric rings indicate the radii from 1 to 5 kpc. The dashed lines draw the crest of the dominant modes determined by Equation (5). Since the halo is rotating in the counterclockwise direction, the dominant waves in (a) are leading, while they are trailing in (b) and (c). The dominant mode is a bar in (d).

sity, velocities, and velocity dispersions remain unchanged, indicating that the system is overall in dynamical equilibrium. At the same time, we also find that the rotating halo allows small-amplitude, non-axisymmetric perturbations to grow in regions with $R \leq 5$ kpc and $|z| \leq 5$ kpc.

To quantify the strength of $m = 2$ perturbations that grow in the halo, we define the Fourier coefficients in $\ln R$ and ϕ as

$$A(m, p) = \frac{1}{N} \sum_{j=1}^N \exp[i(m\phi_j + p \ln R_j)], \quad (5)$$

where N is the total number of particles and (R_j, ϕ_j) are the radial and azimuthal coordinates of the j -th particle in the regions with $R \leq 5$ kpc and $|z| \leq 5$ kpc. In Equation (5), the dimensionless radial wavenumber p is related to the pitch angle $i = \tan^{-1}(m/p)$ of m -armed logarithmic spirals, and $p = 0$ corresponds to a bar mode (e.g., Sellwood & Carlberg 1984; Sellwood & Athanassoula 1986; Oh et al. 2008).

Figure 3 plots the temporal evolution of $|A(2, p)|$ of the $m = 2$ logarithmic spiral waves in the halo-only model with $\lambda = 0.16$ at $t = 0.9$ – 1.1 Gyr. The perturbations are dominated by the mode with $p = -0.6$ at $t = 0.9$ Gyr and $p = 0.8$ at $t = 1.1$ Gyr. The corresponding projected distributions of the $m = 2$ spiral waves, and the loci of the dominant modes are presented in Figure 4(a)–(c). The waves grow as they swing from leading (negative p) to trailing (positive p) configurations.

Figure 5 plots the temporal changes in $|A(2, 0)|$, the strength of a bar mode with $p = 0$, in the halo-only models with $\lambda = 0.16$ (red), $\lambda = 0$ (black), and $\lambda = -0.16$ (blue), as well as its position angle

$$\psi(R) \equiv \frac{1}{2} \tan^{-1} \left[\frac{\sum_j \sin(2\phi_j)}{\sum_j \cos(2\phi_j)} \right], \quad (6)$$

measured at $R = 2$ kpc for the $\lambda = 0.16$ model. When the halo does not spin, the perturbations remain very weak with $|A(2, 0)| \lesssim 5 \times 10^{-3}$, primarily due to Poisson noise in the particle distribution.² However, density perturbations in the rotating halos are swing-amplified to achieve $|A(2, 0)| \sim 0.04$ at $t \sim 2.4$ – 2.8 Gyr in models with $\lambda = \pm 0.16$. The small difference in $|A(2, 0)|$ between the prograde and retrograde halos is presumably caused by the amplitudes of the initial leading perturbations most susceptible to swing amplification.³

Figure 4(d) shows that the spirals eventually grow into a weak bar. By using the cross-correlation of the halo surface densities at two different epochs in the annular regions with width $\Delta R = 0.1$ kpc at $R = 1$ kpc for $t = 2$ – 3 Gyr (see Seo et al. 2019, JK23), we find that the bar in the halo-only model with $\lambda = 0.16$ has a pattern speed of $\Omega_h \sim 6$ km s⁻¹ kpc⁻¹, rotating in the counterclockwise direction. Note that $\Omega_h \approx d\psi/dt$ for $t = 2$ – 3 Gyr shown in Figure 5(b). Similarly, the perturbed density in the retrograde halo with $\lambda = -0.16$ grows first into trailing spirals and then to a bar with a pattern speed of $\Omega_h \sim -6$ km s⁻¹ kpc⁻¹. These indicate that a spinning halo *alone* can form a weak bar that rotates in the same direction as the halo.

Since swing amplification requires self-gravity, rotational shear, and epicyclic shaking (Toomre 1981), it has been studied extensively in the context of galactic disks. However, it can also operate in a spherical system as long as the three agents mentioned above are

² By running models with differing N_h , we have confirmed that $|A(2, 0)| \propto N_h^{-1/2}$ in the models with $\lambda = 0$.

³ Since the initial particle distribution is random, the power spectrum of the corresponding density perturbations is not symmetric in the radial wavenumber p . The leading waves with negative p in the prograde halo become trailing waves with positive p in the retrograde halo.

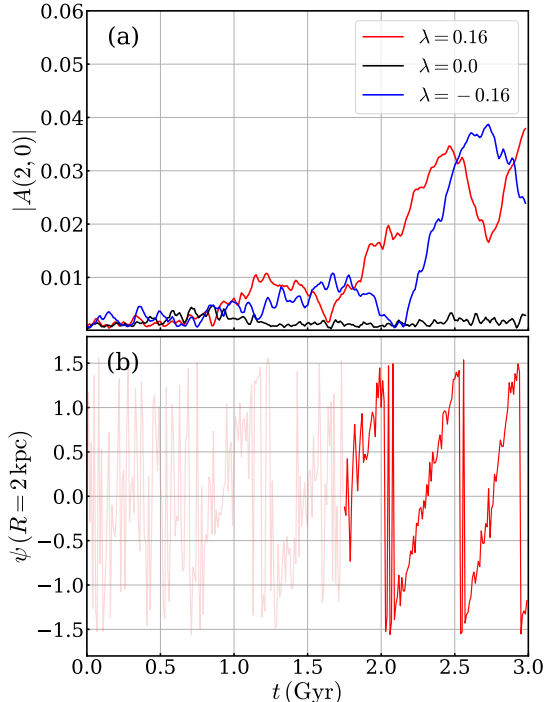


Figure 5. (a) Temporal changes in the strength of the bar mode in the regions with $R \leq 5$ kpc and $|z| \leq 3$ kpc of the halo-only models with $\lambda = 0.16$ (red), $\lambda = 0.0$ (black), and $\lambda = -0.16$ (blue). (b) Temporal evolution of the bar position angle ψ measured at $R = 2$ kpc in the $\lambda = 0.16$ model.

present. As Figure 2 shows, our spinning halo with $\lambda = \pm 0.16$ follows an almost flat rotation curve, indicative of shear and epicyclic motions. By analyzing the orbits of all the halo particles, we find that the fraction of the particles whose orbits are relatively circular with $\max(v_\phi)/\max(v_R) \geq 2$ and remain in the inner regions with $R \leq 5$ kpc close to the midplane with $|z| \leq 5$ kpc is about 0.15% of the halo mass, corresponding to $\sim 10\%$ of the disk mass at $R \leq 5$ kpc. This suggests that swing amplification in the spinning halo can still allow perturbations to grow to produce $m = 2$ spirals and a weak bar, albeit much weaker than a strong bar that forms in the disk.

To summarize, our rotating halo in itself is vulnerable to the formation of non-axisymmetric structures. Small-amplitude (internal) perturbations in a spinning halo grow due to swing amplification into spirals and then to a bar which rotates in the same sense as the halo. As we will show in Section 4, this tendency of a spinning halo forming non-axisymmetric structures even without external perturbations promotes or delays the bar formation in a stellar disk depending on its direction of rotation relative to the halo.

4. FULL GALAXY MODELS

We now present the simulation results of full galaxy models with halo and disk listed in Table 1. We first focus on the bar formation and evolution in our models, and then explore the bar pattern speed, angular momentum transport, and vertical buckling instability.

4.1. Bar Formation and Evolution

All of our models produce bars in the disks. The bar formation is due to successive swing amplification aided by feedback loops (e.g., Binney & Tremaine 2008): small-amplitude perturbations in a stellar disk grow as they transition from a leading to a trailing configuration, and trailing waves appear as leading waves after they pass through the galaxy center. In the growing stage, they interact gravitationally with the particles in the halo and bulge, and the halo spin certainly affects the wave growth. When the waves grow sufficiently, they shape into a bar. Figure 6 plots snapshots of the disk surface density for models at every 0.1 Gyr interval from $t = 0.1$ to 1.8 Gyr in models C00P00 (top), C00P16 (middle), and C00R16 (bottom).

We follow the method of Kataria & Das (2018) to measure the strength of a bar that forms in the disk (see also JK23). We consider an annulus centered at radius R with width $\Delta R = 1$ kpc in the regions with $R \leq 10$ kpc of the disk, and calculate the amplitudes of the Fourier modes as

$$a_m(R) = \sum_j \mu_j \cos(m\phi_j), \quad (7a)$$

$$b_m(R) = \sum_j \mu_j \sin(m\phi_j), \quad (7b)$$

where ϕ_j and μ_j are the azimuthal angle and mass of the j -th disk particle in the annulus, respectively. Then we define the strength of the density perturbations with mode m as the maximum wave amplitude across all annuli:

$$\frac{A_m}{A_0} = \max_R \left\{ \frac{[a_m(R)^2 + b_m(R)^2]^{1/2}}{\sum_j \mu_j} \right\}. \quad (8)$$

Note that the term inside the curly brackets in Equation (8) is equal to $|A(m,0)|$ defined in Equation (5) if the particles have the same mass.

Figure 7 plots the temporal evolution of A_2/A_0 and A_3/A_0 at early time ($t \leq 2$ Gyr) for models C00P00 (black), C00P16 (red), and C00R16 (blue). In model C00P00 with no halo spin, the disk favors the growth of $m = 2$ and 3 spirals, with the $m = 3$ mode dominating at $t \lesssim 0.8$ Gyr (see the top row of Figure 6). These modes with different m interact nonlinearly with each other, and one arm of the $m = 3$ spirals merges with

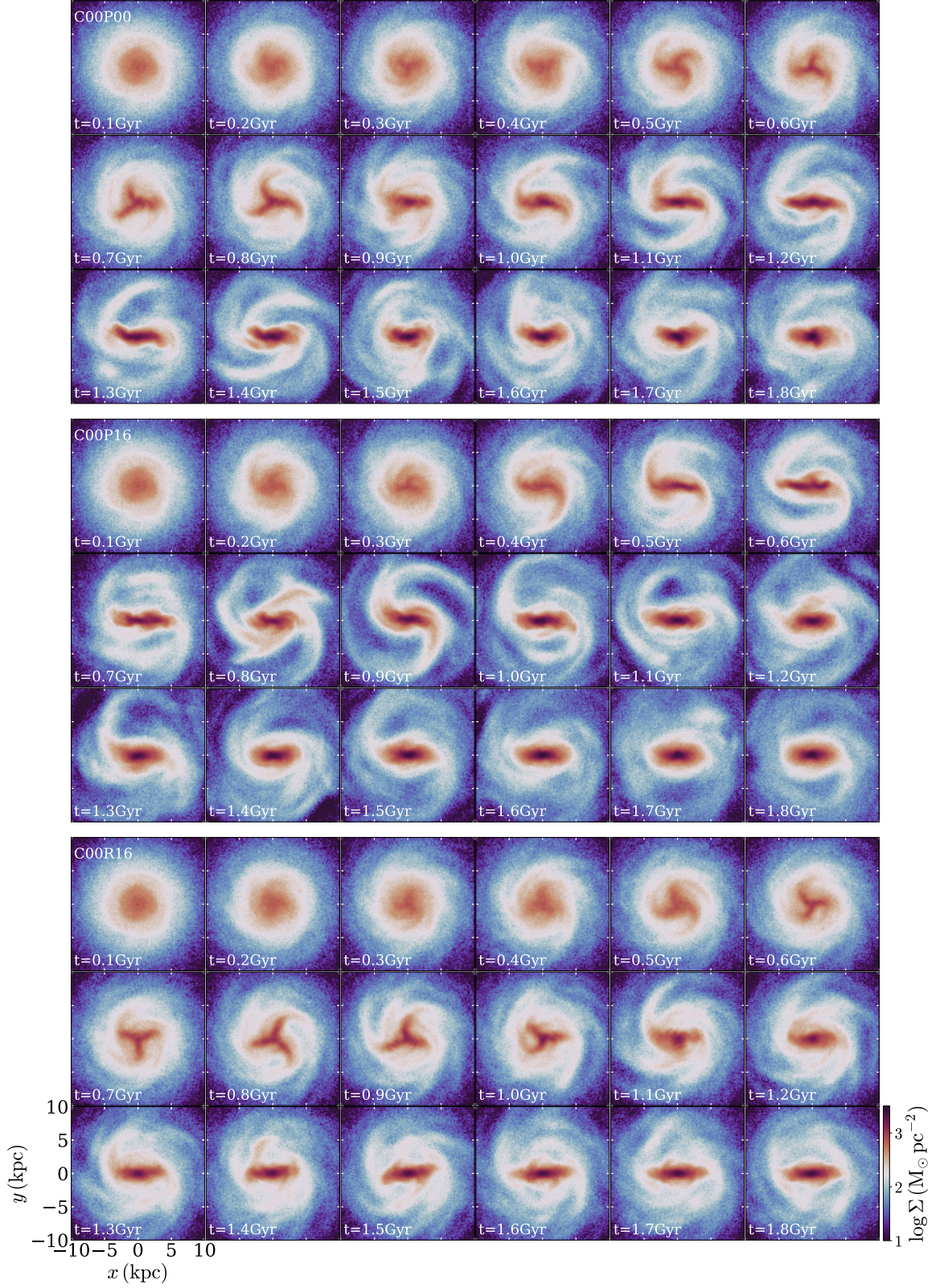


Figure 6. Snapshots of the disk surface density at every 0.1 Gyr interval from $t = 0.1$ to 1.8 Gyr in models C00P00 with non-spinning halo (top), C00P16 with a prograde halo (middle), and C00R16 with a retrograde halo (bottom).

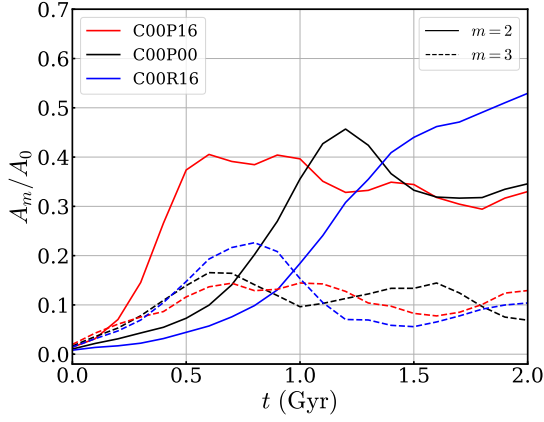


Figure 7. Temporal evolution of A_2/A_0 (solid) and A_3/A_0 (dashed) for models C00P00 (black), C00P16 (red) and C00R16 (blue) at early time ($t \leq 2$ Gyr).

the other two arms, producing a bar at $t \sim 0.9$ Gyr (see also, [Seo et al. 2019](#)). The $m = 3$ mode in these models decays secularly to become $A_3/A_0 \sim 3 \times 10^{-2}$ at the end of the runs ($t = 10$ Gyr).

In model C00P16 with $\lambda = 0.16$, the growth of the $m = 2$ mode in the disk is assisted by the prograde halo which has an intrinsic tendency of amplifying the $m = 2$ perturbations rotating in the same sense as the halo. Consequently, the $m = 2$ spirals in this model become stronger and thus transform to a bar earlier ($t \sim 0.5$ Gyr) than in model C00P00 (see the middle row of [Figure 6](#)). We note that the regions outside the bar in model C00P16 are more strongly perturbed by the $m = 2$ spirals than in model C00P00, limiting further growth of the bar. In model C00R16 with $\lambda = -0.16$, in contrast, the growth of the $m = 2$ mode in the disk is opposed to some extent by the counter-rotating halo, which in turn allows for the $m = 3$ mode to grow more strongly than in model C00P00. Therefore, it takes longer for the $m = 3$ spirals to transform eventually into a bar than under the non-spinning halo.

[Figure 8](#) plots the temporal evolution of A_2/A_0 for C00 series (upper panel) and C10 series (lower panel) over entire evolution. The bar in model C00P16 stops growing at $t \sim 1.0$ Gyr. At this time, the inner parts of the spirals dominating the outer regions become in phase with the bar, making A_2/A_0 increase temporarily to ~ 0.4 . As the spirals rotate relative to the bar and become out of phase, A_2/A_0 decreases to ~ 0.32 at $t \sim 2$ Gyr. Since the regions outside the bar are strongly perturbed by the $m = 2$ spirals, they do not participate in the bar growth, making A_2 stay almost constant for a long period. The bar undergoes a weak buckling instability at $t \sim 9.5$ Gyr (see [Section 4.3](#)).

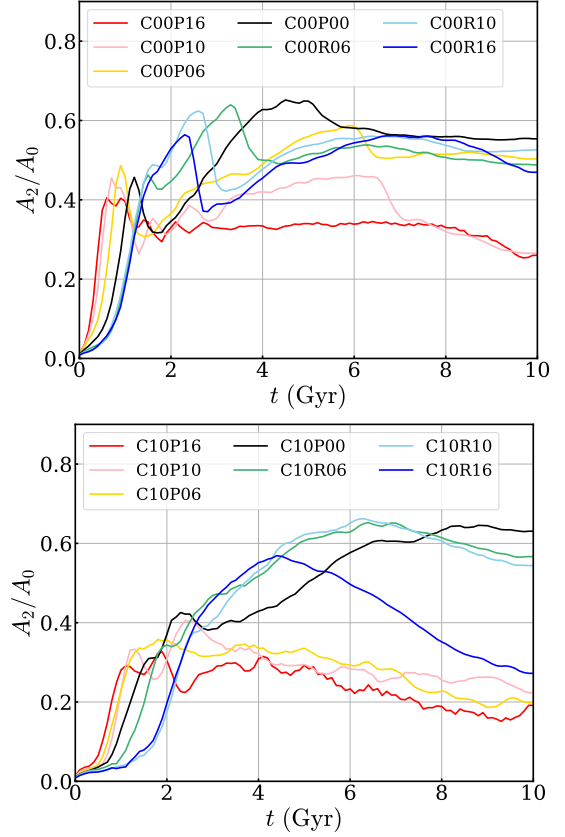


Figure 8. Temporal evolution of the bar strength A_2/A_0 for the C00 series (top) and C10 series (bottom) for $t \leq 10$ Gyr. A bar tends to form early under a prograde halo and without bulge.

In model C00P00 with no halo spin, A_2/A_0 peaks near $t \sim 1.1$ Gyr when the spirals are in phase with the bar, after which A_2/A_0 decreases as the bar becomes out of phase with the spirals. Since the regions outside the bar possess weaker spirals and are thus less disturbed than in model C00P16, the bar in this model can grow in size and strength by gathering outer particles until it undergoes a buckling instability at $t \sim 5.2$ Gyr. In model C00R16 with a counter-rotating halo, the bar grows slower but more strongly than the other models since the spiral perturbations in the outer regions are weakest. The bar becomes so strong that the buckling instability occurs at $t \sim 2.5$ Gyr, earlier than the other models.

The models in the C10 series with a classical bulge also form a bar, but later than the no-bulge counterparts. This is because the gravity of a bulge reduces the feedback loop and swing amplification. The bars in the C10 series are weaker and shorter at early time ($t \lesssim 2$ Gyr) than those in the C00 series, indicating that the presence of a non-rotating bulge, in general, resists the bar formation ([Sellwood 1980](#); [Binney & Tremaine 2008](#); [Kataria & Das 2018](#); [Saha & Elmegreen 2018](#); [JK23](#)).

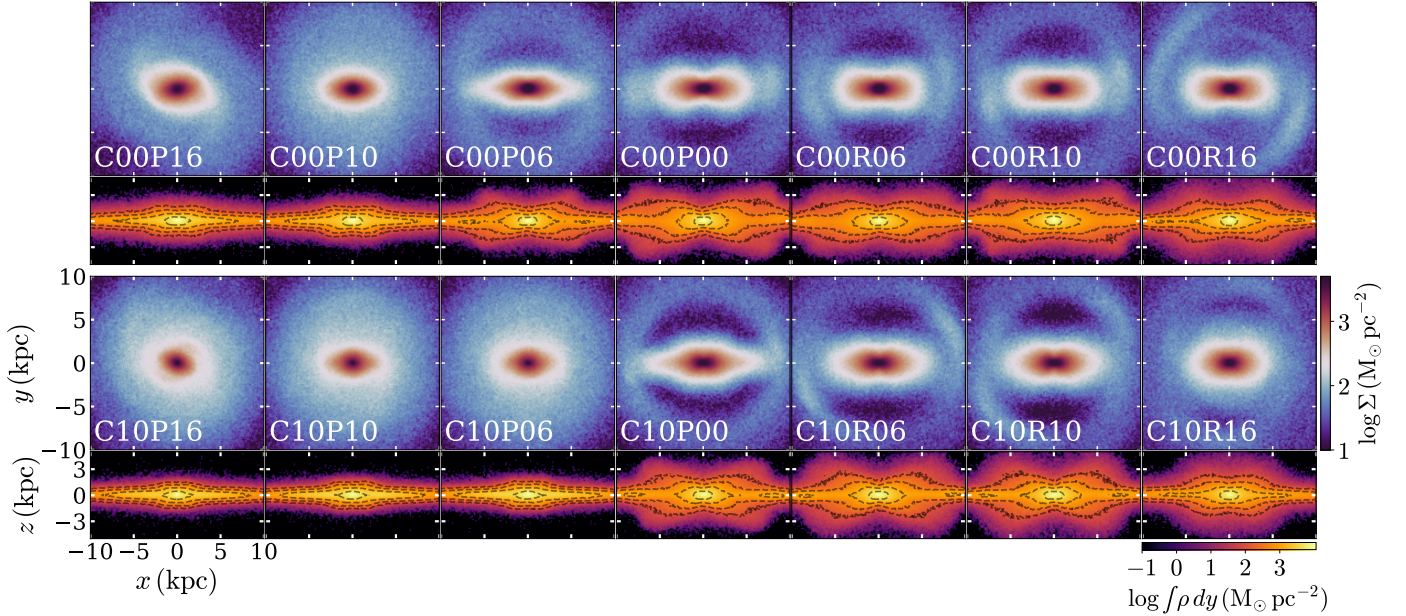


Figure 9. Snapshots of the disk surface density (top) and the projected disk density along the bar semi-minor axis (bottom) at the end of the runs ($t = 10$ Gyr) for all models. The upper and lower rows correspond to the models in the C00 and C10 series, respectively. The x - and y -axis correspond to the semi-major and semi-minor axis, respectively. In the edge-on views, the dotted contours denote $\int \rho dy = 10^{3.5}, 10^{3.0}, 10^{2.5}, 10^{2.0} M_{\odot} \text{pc}^{-2}$ from inside to outside.

The bars in models C10P16, C10P10 and C10P06 are always weaker than those in the no-bulge counterparts. However, the bars in the other models with a bulge do not undergo buckling instability and can thus be stronger than those without a bulge. For example, the bar in model C10P00 keeps growing to reach $A_2/A_0 \sim 0.64$, while the bar in model C00P00 suddenly becomes weaker after experiencing buckling instability at $t \sim 5.2$ Gyr.

Figure 9 plots the snapshots of the disks projected along the vertical direction and the bar semi-minor axis at $t = 10$ Gyr for all models. The bar rotating in the counterclockwise direction is oriented so that the x - and y -axes correspond to the semi-major and semi-minor axes, respectively. The bar in model C00P16 shows a twist of isodensity contours in the outer parts. The bar in model C10P16 is so weak that it can be regarded as an oval. The surface density near the center has a dumbbell-like distribution only in model C00P00. The models with relatively strong bars (other than models C00P16, C00P10, C10P16, C10P10 and C10P06) possess a boxy peanut-shaped (BPS) bulge as well as an inner ring just outside the bar.

4.2. Angular Momentum and Bar Pattern Speed

After formation, a bar embedded in a disk transfers its angular momentum to a halo (and a bulge). To study the radial and temporal dependence of the angular momentum transfer, we bin each component radially into

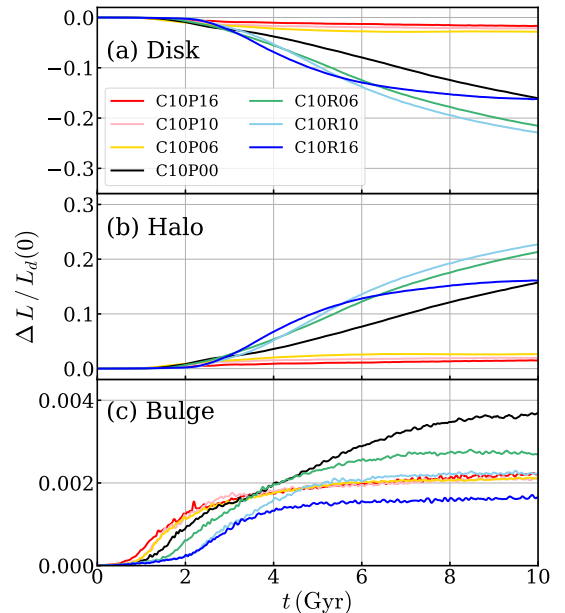


Figure 10. Temporal changes in the angular momentum $\Delta L \equiv L(t) - L(0)$ of the entire disk (top), halo (middle), and bulge (bottom) for the models in the C10 series. The ordinate is normalized by the initial angular momentum of the entire disk.

concentric cylindrical shells with width $\Delta R = 1$ kpc and calculate the vertical component of the angular momentum

$$L = \sum_i \mu_i (x_i v_{y,i} - y_i v_{x,i}) \quad (9)$$

in each shell. Figure 10 plots $\Delta L \equiv L(t) - L(0)$ summed over the entire shells as a function of time for the models in the C10 series. Overall, the amount of angular momentum absorbed by the bulge is much less than that by the halo. The disk under a counter-rotating halo loses more angular momentum than under the prograde halo, making the bar in the former grow stronger and longer at the end of the runs (see Figure 9). Of course, the actual temporal change of ΔL depends on not only λ but also the bar properties such as strength, length, pattern speed, mass distribution, etc.

Figure 11 displays the rate of angular momentum transfer, dL/dt , as a function of R and t in the halo and disk for models C00P16, C00P00, and C00R16. When $\lambda > 0$, the halo particles inside the corotation resonance R_{CR} with the bar rotate faster than, and thus lose their angular momenta to the bar, while the particles in the outer halo gain angular momentum (Long et al. 2014; Collier et al. 2018). Since R_{CR} is larger for larger λ , the angular momentum transfer from disk to halo tends to be larger for smaller $\lambda > 0$. In model C00P16, most angular momentum transfer occurs near $t \sim 1$ Gyr when the bar is strongest. The bar angular momentum is also transferred to the outer disk at $R > R_{\text{CR}}$.

When $\lambda \leq 0$, in contrast, all the halo particles lag behind the bar and thus allow the efficient angular momentum transfer. Figure 11 shows that the halo in model C00P00 absorbs angular momentum mainly through three resonances which extend radially outward as the bar grows in size over time (e.g., Villa-Vargas et al. 2009; Collier et al. 2018, 2019a,b). Again, the largest dL/dt occurs near $t \sim 3\text{--}5$ Gyr when the bar is strongest. The outer disk absorbs the angular momentum emitted by the bar. The halo in model C00R16 absorbs angular momentum strongly at $t \sim 1\text{--}3$ Gyr and $\sim 5\text{--}7$ Gyr, corresponding to a strong bar before the buckling instability and in the regrowth stage (see Figure 8).

We calculate the bar pattern speed, Ω_b , using the cross-correlation of the disk surface density in the annular regions with width $\Delta R = 0.1$ kpc at $R = 2$ kpc: we check that the resulting Ω_b agrees within $\sim 1\%$ with that from the method that utilizes the temporal changes in the bar position angle $\psi = 0.5 \tan^{-1}(b_2/a_2)$ (JK23). Figure 12 plots the temporal changes in the bar pattern speed for all models. As the bar loses its angular momentum to the halo and bulge, its pattern speed decreases over time. The initial bar pattern speed tends to be higher in models with a prograde halo and with a bulge. This is consistent with the numerical results that a short bar tends to rotate fast (Aguerri et al. 2015; Roshan et al. 2021; Lee et al. 2022; Frankel et al. 2022;

JK23). Note that the bar slows down very slowly in models with $\lambda = 0.16$ since the angular momentum absorption by the halo outside R_{CR} is almost balanced by the angular momentum emission by the halo inside R_{CR} . Models with smaller $\lambda (> 0)$ have smaller R_{CR} and thus causes Ω_b to decay faster over time. This is qualitatively consistent with the analytic result of Chiba & Kataria (2024) who showed that the dynamical friction of a bar due to halo particles weakens with increasing halo spin. Models with $\lambda < 0$ have Ω_b decreasing more or less similarly to that in the $\lambda = 0$ models, largely consistent with the result of Collier et al. (2019a) in that the amount of angular momentum transport is insensitive to λ as long as the halo has a retrograde spin.

4.3. Buckling Instability

All the bars in our models thicken vertically over time, evolving into a BPS bulge if strong. The BPS strength is usually defined as

$$P_s = \max_R \left(\frac{|\widetilde{z}|}{|\widetilde{z}_0|} \right), \quad (10)$$

where the tilde denotes the median and z_0 is the initial height for the disk particles at $R \leq 10$ kpc (Iannuzzi & Athanassoula 2015; Fragkoudi et al. 2017; Seo et al. 2019). Figure 13 plots temporal evolution of P_s for all models. Note that the models in the C00 series with no bulge (except for model C00P16) go through a short period where P_s increases rapidly due to buckling instability. In contrast, P_s in the models in the C10 series with a bulge does not experience such a rapid increase. Instead, it increases relatively slowly due to the vertical heating of disk particles via gravitational interactions with the bar without undergoing buckling instability.

Figure 14 compares the projected disk densities along the bar semi-minor axis in models C00P00 (left) and C10P00 (right) for $t = 4.5\text{--}7.0$ Gyr. Clearly, the bars in both models produce a BPS bulge. Note that the projected disk densities in model C00P00 become asymmetric with respect to the $z = 0$ plane at $t \sim 5.5$ Gyr, indicative of the buckling instability. However, the bar in model C10P00 almost always maintains a mirror symmetry about the midplane, while it gradually thickens vertically. This relatively slow thickening of the bars can be caused by 2:1 and 4:1 vertical resonances (Combes et al. 1990; Pfenniger & Friedli 1991; Patsis et al. 2002; Sellwood & Gerhard 2020). This indicates that the buckling instability is not a necessary but sufficient condition for forming a BPS bulge (Li et al. 2023).

Since the buckling instability deforms the disk in the vertical direction, it naturally involves the asymmetry in the vertical velocities of disk particles. One way to

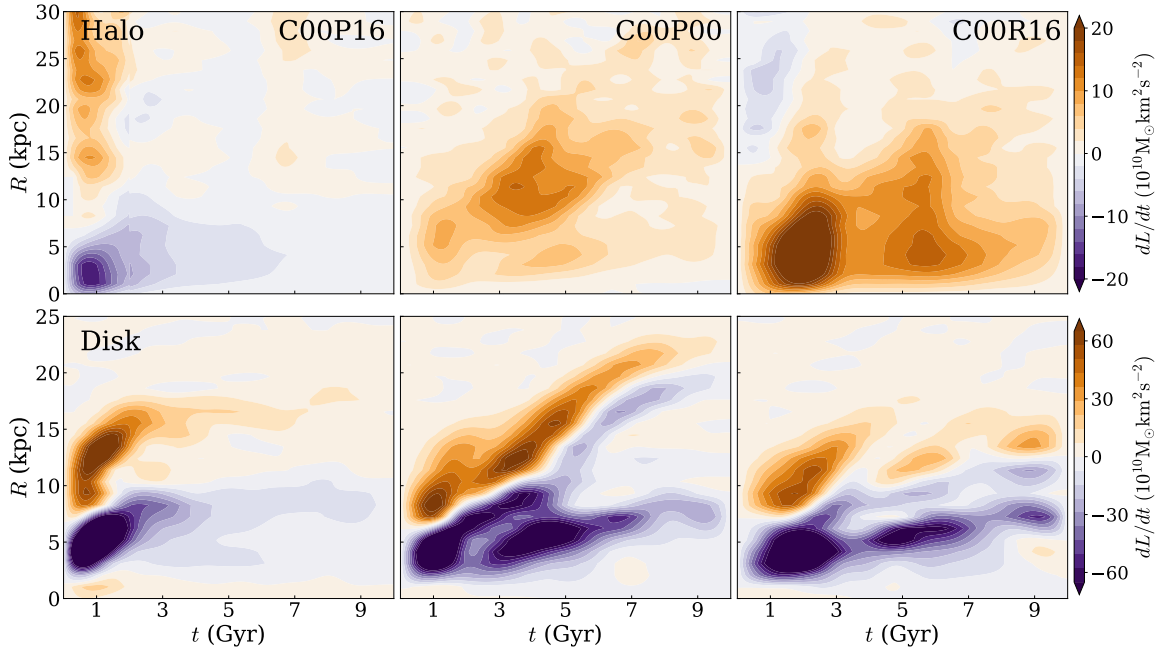


Figure 11. Rates of the angular momentum change, dL/dt , as a function of cylindrical radius and time for models C00P16 (left), C00P00 (middle), and C00R16 (right). The cylindrical shells have a width $\Delta R = 1$ kpc and height $|z| = \infty$ for the halos (upper panels) and the stellar disks (lower panels).

quantify the onset and strength of the buckling instability is to monitor the evolution of $|\langle v_z \rangle|$, where the angle brackets denote the spatial average at $R = 2$ kpc (Kwak et al. 2017, 2019). Figure 15 plots $|\langle v_z \rangle|$ against time for all models. A sharp peak in $|\langle v_z \rangle|$ corresponds to the buckling instability, which starts to occur at $t = 2.5, 2.9, 3.7, 5.2, 6.2, 6.8$ Gyr for models C00R16, C00R10, C00R06, C00P00, C00P06, C00P10, respectively. Model C00P16 also undergoes a buckling instability at $t \sim 9.5$ Gyr, although it is very mild. The bottom panel of Figure 15 shows that $|\langle v_z \rangle|$ of the models in the C10 series exhibit only noises, suggesting that they do not experience buckling instability at all.

Another way to measure the strength of the buckling instability is to use the vertical asymmetry parameter of the disk introduced by Smirnov & Sotnikova (2018) as

$$A_{\text{asym}} = \left| \frac{A_2(z > 0) - A_2(z < 0)}{A_0} \right|, \quad (11)$$

where $A_2(z > 0)$ and $A_2(z < 0)$ denote the Fourier amplitudes of the $m = 2$ mode applied to the disk particles above and below the $z = 0$ plane, respectively (see also Li et al. 2024). Figure 16 plots A_{asym} from all the disk particles (left) as well as the particles located at $R \leq 5$ kpc (right). The models with no bulge have A_{asym} varying a lot over time, while A_{asym} for the models with a bulge is close to zero. For the models without a bulge, A_{asym} from the entire disk exhibits longer-term variations than that from the regions with $R \leq 5$ kpc,

suggesting that the buckling instability initiates from smaller radii and propagates radially outward. Compared to $|\langle v_z \rangle|$, A_{asym} for the models in the C00 series are more widely distributed over time. This is because A_{asym} captures the asymmetry in a wider radial range and the buckling instability occurs in the inner disk first and then propagates outward (Martinez-Valpuesta et al. 2006). Note that $|\langle v_z \rangle|$ can be small if the nodes of the vertical bending in the course of buckling are located close to $R = 2$ kpc, as in models C00P00, C00P06, and C00P10. This suggests that the peak values of A_{asym} represent the overall strength of the buckling instability better than $|\langle v_z \rangle|$.

As Figures 15 and 16 show, the buckling instability occurs earlier in our models with smaller λ , that is, as the fraction of retrograde halo particles increases. This trend is not observed in previous investigations (Long et al. 2014; Collier et al. 2018, 2019a,b; Kataria & Shen 2022). In Collier et al. (2018, 2019a), the maximal pre-buckling amplitude of A_2/A_0 is almost insensitive to $\lambda > 0$, while it becomes smaller as λ decreases in the models with a retrograde halo. In our models, the pre-buckling strength is most significant in the models with $\lambda = 0$ and decreases as $|\lambda|$ increases in models with either a prograde or retrograde halo (see Figure 8).

It is well known that the buckling instability occurs when the radial velocity dispersion σ_R of disk particles exceeds a critical value relative to the vertical velocity dispersion σ_z (e.g., Binney & Tremaine 2008). Toomre

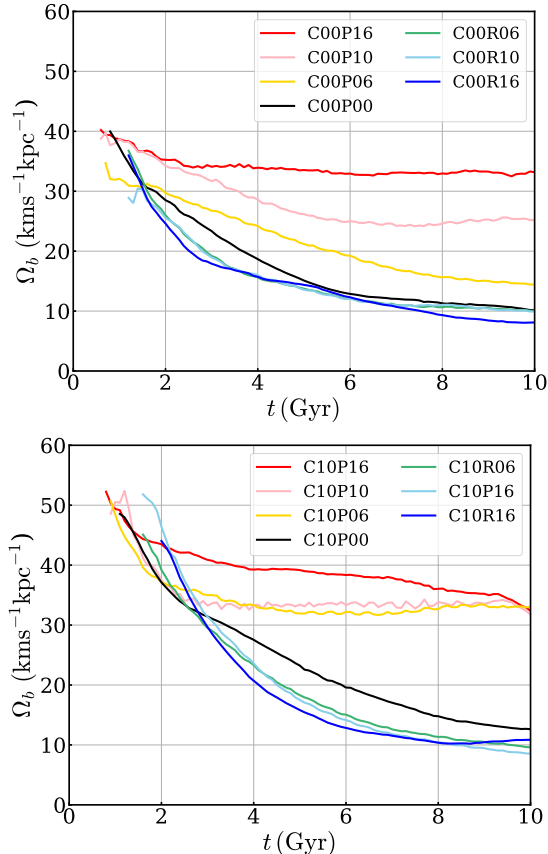


Figure 12. Temporal changes of the bar pattern speed Ω_b for the C00 series (top) and C10 series (bottom).

(1966) and Araki (1987) found that the critical value is at $\sigma_z/\sigma_R \sim 0.3$ for non-rotating, razor-thin disks. For realistic disks with spatially-varying σ_z/σ_R , Raha et al. (1991) found that the disks undergo buckling instability when $\sigma_z/\sigma_R \lesssim 0.25\text{--}0.55$. For barred galaxies, N -body simulations of Martinez-Valpuesta et al. (2006) and Kwak et al. (2017) found that buckling occurs when $\sigma_z/\sigma_R \lesssim 0.6$.

Figure 17 plots the temporal changes in σ_z/σ_R of the disk particles at $R = 2$ kpc for the models in the C00 series (top) and the C10 series (bottom). For most of the models without a bulge, the onset of the buckling instability corresponds to $\sigma_z/\sigma_R \simeq 0.47\text{--}0.60$. Note that model C00P16 has $\sigma_z/\sigma_R \sim 0.75$ at $t = 9.5$ Myr, but it still exhibits mild buckling instability, as evidenced by the asymmetry parameter shown in Figure 16. All the models with a bulge have $\sigma_z/\sigma_R \gtrsim 0.55$, and remain stable against buckling instability. Instead, the bars in these models thicken gradually to produce BPS bulges (see Figure 14). This indicates that the critical value of σ_z/σ_R for buckling instability is applicable only to the models without a bulge.

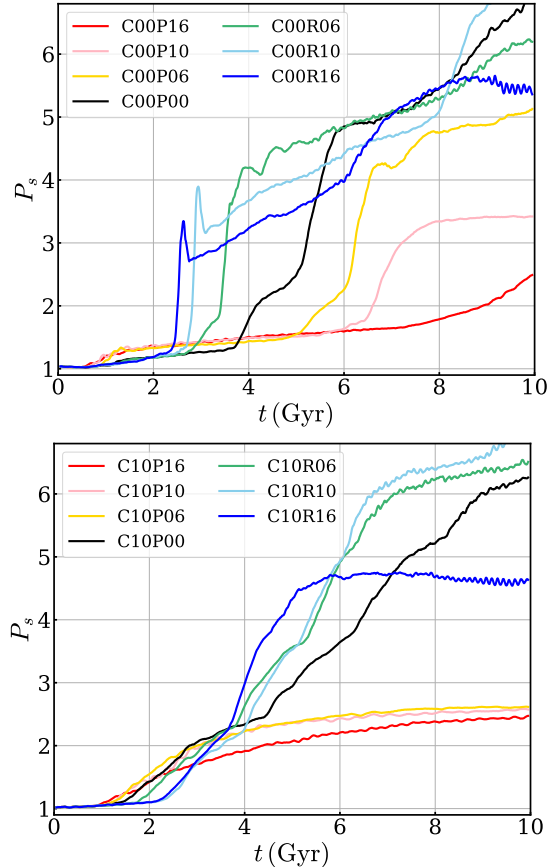


Figure 13. Time evolution of the BPS strength, P_s , defined in Equation (10) for the models in the C00 series with no bulge (top) and C10 series with a bulge (bottom).

5. DISCUSSION

We have investigated the formation and evolution of bars in disk galaxies similar to the Milky Way, with a spinning halo. In this section, we discuss our results compared to the previous investigations. We also use the bar properties to constrain the models for the Milky Way.

5.1. Bar Formation under a Spinning Halo

In our models, a disk embedded in a faster corotating halo develops a bar earlier, while the bar formation is delayed under a counter-rotating halo, consistent with the results of the previous studies (Saha & Naab 2013; Long et al. 2014; Collier et al. 2018, 2019a). As mentioned in Section 1, Saha & Naab (2013) tried to explain this in terms of the Ostriker-Peebles parameter t_{OP} , arguing that the halo spin increases t_{OP} and thus makes the disk more susceptible to bar formation. Since t_{OP} does not consider the sense of halo rotation, however, it cannot explain why a bar forms faster in a disk under a prograde halo than under the retrograde counterpart.

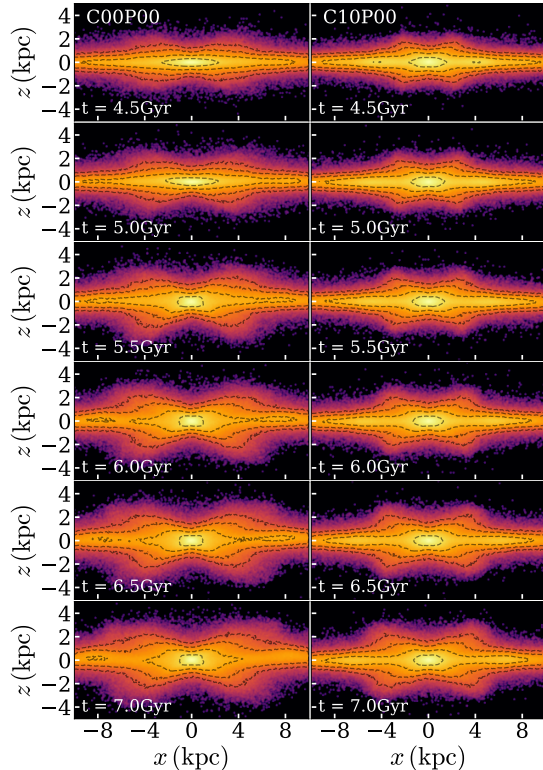


Figure 14. Contours of the logarithm of the projected disk densities at $t = 4.5$ – 7.0 Gyr for models C00P00 (left) and C10P00 (right). The buckling instability occurs at $t \sim 5.5$ Gyr in model C00P00. The x - and z -axis correspond to the bar semi-major and vertical axes, respectively. The dotted contours denote $\int \rho dy = 10^{3.5}, 10^{3.0}, 10^{2.5}, 10^{2.0} M_{\odot} \text{pc}^{-2}$ from inside to outside.

To account for the disk response to a spinning halo, we examine the growth of various modes in an isolated halo and a disk-halo system. In Section 3, we present that our spinning halo alone is vulnerable to the growth of $m = 2$ spirals due to swing amplification, transforming to a weak bar rotating in the same sense as the halo. When a disk is inserted into the halo, $m = 2$ spirals in the disk growing also via swing amplification supply gravitational perturbations for the halo. If the halo spin is prograde, the perturbations are well maintained and amplified in the halo, giving positive feedback to the spirals in the disk. Therefore, the disk and the prograde halo work constructively to make the spirals grow faster than in the case with no halo spin, promoting the bar formation (see Figure 7). If the halo spin is instead retrograde, $m = 2$ perturbations in the disk and halo become out of phase and interact destructively. In this case, the $m = 2$ spirals in the disk grow more slowly, delaying the bar formation.

5.2. Buckling Instability

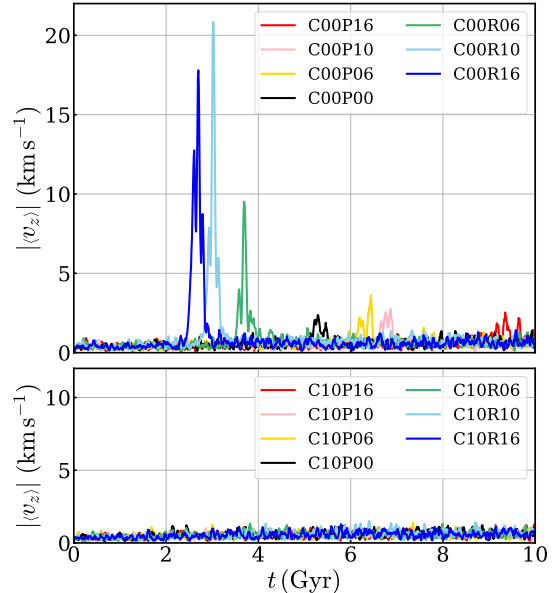


Figure 15. Temporal evolution of the mean vertical velocity $|\langle v_z \rangle|$ at $R = 2.0$ kpc of the disk for the models in the C00 series (top) and the C10 series (bottom).

Numerical simulations commonly found that bars undergo vertical buckling instability when sufficiently strong, resulting in weakened and shorted bars and eventually leading to BPS bulges. Our simulations also show that strong bars are subject to buckling instability. There are, however, some discrepancies between the results of our models and the previous simulations (Saha & Naab 2013; Long et al. 2014; Collier et al. 2018, 2019b). First, in models of Collier et al. (2018, 2019a,b), there is no apparent correlation between λ and the epoch of the buckling instability, while the buckling in our models is progressively delayed with increasing λ . Second, the bar strength before the buckling instability is almost independent of λ in models with a prograde halo (Collier et al. 2018, 2019b) and decreases with λ in models with a retrograde halo (Collier et al. 2019a), while it is a decreasing function of $|\lambda|$ for the whole range of λ in our models (see Figure 8). Third, the buckling instability almost destroys the bars when $\lambda \gtrsim 0.06$ in Collier et al. (2018, 2019b), while the bars, albeit becoming weaker, still remain strong after the buckling in our models. Lastly, our models with a bulge do not undergo buckling instability at all, while the models even with a bulge in Li et al. (2024) experience buckling instability, although the onset and amplitude of the buckling decrease with increasing bulge mass.

It is uncertain what causes these differences in the numerical results, but the most likely reason may be differences in the galaxy models adopted. Our models consider a Milky Way-sized galaxy, while the previous

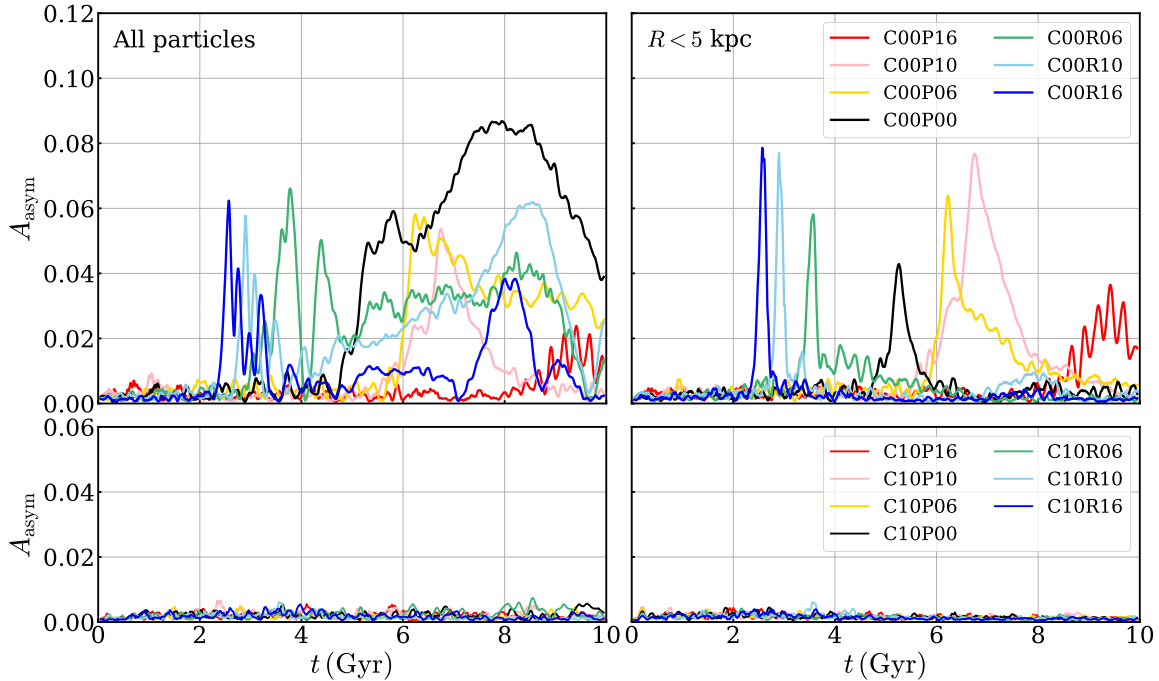


Figure 16. Temporal evolution of the vertical asymmetry parameter A_{asym} , defined in Equation (11), from all the disk particles (left) and the particles at $R < 5$ kpc (right) for the models in the C00 series (top) and the C10 series (bottom).

authors (Long et al. 2014; Collier et al. 2018, 2019a,b; Collier & Madigan 2021; Li et al. 2024) employed the models with a twice less massive halo and a twice thicker disk than our models. Also, their halo modeled by a truncated NFW profile (Navarro et al. 1996) has a different degree of central concentration and a quite different rotation curve from ours (e.g., Figure 1 in the present work can be compared with Figure 1 of Lieb et al. 2022). These suggest that one should be cautious about drawing a general conclusion by running a limited set of numerical simulations.

The firehose instability has been invoked as the physical mechanism behind the buckling instability (Toomre 1966; Binney & Tremaine 2008). An alternative mechanism may be the trapping of overlapped planar and vertical 2:1 resonances, proposed recently by Li et al. (2023). In the firehose instability, bending perturbations become unstable if the centrifugal force on stars traveling over corrugations exceeds the restoring gravitational force from the other stars, which is achieved when σ_z/σ_R becomes less than a critical value (see e.g., Combes & Sanders 1981; Combes et al. 1990; Raha et al. 1991; Merritt & Sellwood 1994; Martinez-Valpuesta et al. 2006; Kwak et al. 2017, 2019; Li et al. 2024, and references therein). Our simulations show that the buckling instability in strongly barred galaxies occurs when $\sigma_z/\sigma_R \lesssim 0.47\text{--}0.60$, roughly consistent with the results of Martinez-Valpuesta et al. (2006) and Kwak et al. (2017).

The buckling instability in most of our models is consistent with the conventional picture that it needs $\sigma_z/\sigma_R < 0.6$ for operation and that it increases σ_z/σ_R rapidly, while decreasing A_2/A_0 , as Figures 8 and 17 show. However, the buckling instability in model C00P16 is exceptional in that it works even with $\sigma_z/\sigma_R \sim 0.75$ and does not cause a sharp increase in σ_z/σ_R and bar weakening. Figure 18 compares the face-on snapshots of the mean vertical velocities, \bar{v}_z , and the mean vertical positions, \bar{z} , of the disk particles for models C00R16 (left) and C00P16 (right) each at the epoch of the maximum buckling. Model C00R16 which undergoes strong buckling at $t \sim 2.7$ Gyr exhibits characteristic quadrupole patterns in the face-on maps, with $|\bar{v}_z| \lesssim 30$ km s $^{-1}$ and $|\bar{z}| \lesssim 0.5$ kpc (see, e.g., Lokas 2019; Xiang et al. 2021; Li et al. 2023). Note that model C00P16 also shows similar quadrupole patterns, although they are weaker with $|\bar{v}_z| \lesssim 10$ km s $^{-1}$ and $|\bar{z}| \lesssim 0.2$ kpc, demonstrating that it indeed suffers the buckling instability near $t \sim 9.7$ Gyr. One cannot rule out the possibility of overlapping planar and vertical 2:1 resonances, as envisaged by Li et al. (2023), for the nature of the buckling instability in model C00P16.

5.3. Milky Way Bar

We now discuss which of our models best describes the properties of the Milky Way bar. Observations show that the Milky Way bar is long with size $R_b \sim 4.5\text{--}5$ kpc and rotates slowly with pattern speed $33 < \Omega_b <$

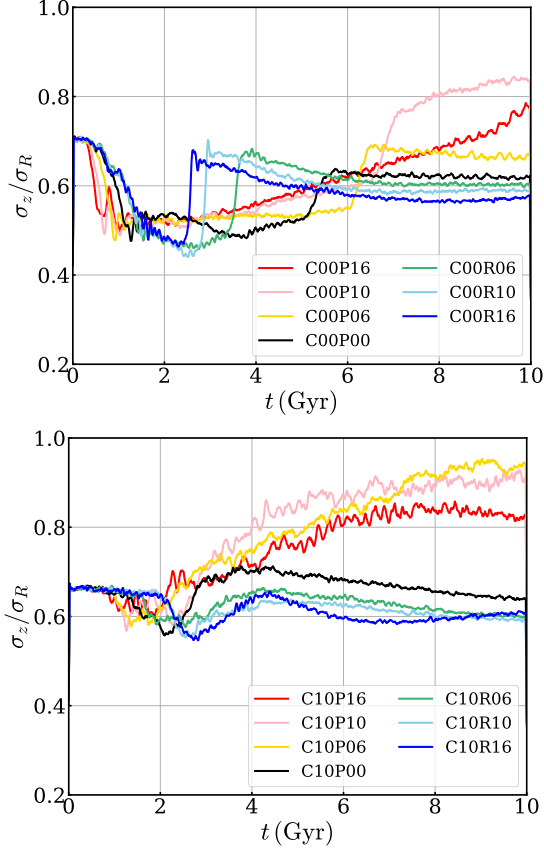


Figure 17. Temporal variations of the ratio σ_z/σ_R of the vertical to radial velocity dispersion of the disk particles at $R = 2$ kpc for the models in the C00 series (top) and the C10 series (bottom).

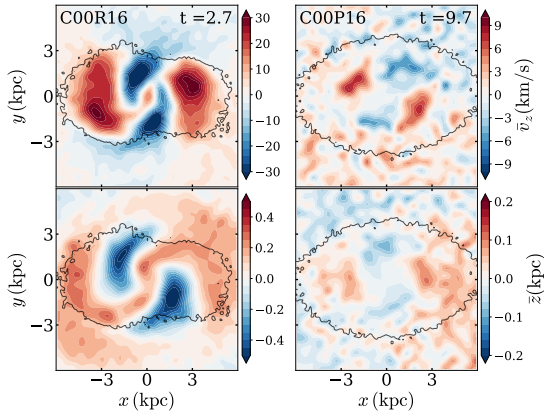


Figure 18. Face-on maps of the mean vertical velocities (top) and mean vertical positions (bottom) of the stars at $t = 2.7$ Gyr for model C00R16 (left) and at $t = 9.7$ Gyr for model C00P16 (right). The contour in each panel outlines the bar boundaries defined as the regions with $\Sigma = 2 \times 10^2 M_\odot \text{pc}^{-2}$.

$45 \text{ km s}^{-1} \text{ kpc}^{-1}$ (Wegg et al. 2015; Sormani et al. 2015; Portail et al. 2017; Bland-Hawthorn & Gerhard 2016;

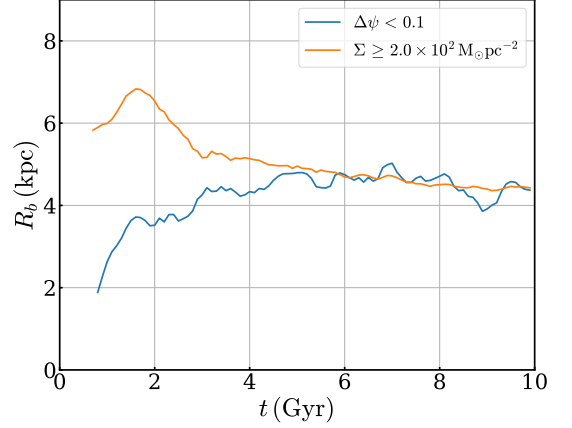


Figure 19. Temporal evolution of the bar length R_b in model C10P06. The blue line corresponds to R_b calculated by imposing the changes of the position angle $\Delta\psi \leq 0.1$ of the $m = 2$ mode, while the orange line is obtained by defining the bar as the regions with $\Sigma \geq 2 \times 10^2 M_\odot \text{pc}^{-2}$.

Clarke & Gerhard 2022). Measuring the spin parameter λ of a galaxy is a difficult task observationally. Recently, Obreja et al. (2022) found a correlation between the angular momenta of dark halos and disks from a sample of galaxies identified in cosmological simulations, and used the relation to estimate λ_{MW} of the Milky Way after measuring its disk angular momentum. They obtained $\lambda_{\text{MW}} \sim 0.061$ when the dark halo of the Milky Way follows a contracted NFW profile, and $\lambda_{\text{MW}} \sim 0.088$ for an uncontracted profile.

JK23 found that models C10 and C20 with $\lambda = 0$, containing a classical bulge with mass 10% and 20% of the disk mass, respectively, match the properties of the Milky Way bar quite well. This suggests that model C10P06 in the present paper best represents the Milky Way when the halo spin is considered. Indeed, Figure 12 shows that the bar in model C10P06 has $\Omega_b \sim 30\text{--}35 \text{ km s}^{-1} \text{ kpc}^{-1}$ for a long period of time. Figure 19 plots the temporal changes of the bar length calculated from two methods: (1) the maximum radius where the change in the bar position angle $\Delta\psi < 0.1$ and (2) the semi-major axis with $\Sigma \geq 2 \times 10^2 M_\odot \text{pc}^{-2}$. The bar length of $R_b \sim 4\text{--}5$ kpc at $t \gtrsim 3$ Gyr is consistent with the observed size of the Milky Way bar. That R_b from $\Delta\psi$ is longer than that from Σ at $t \lesssim 4$ Gyr is due to the temporal alignment of the inner parts of the spirals with the bar ends.

We remark on some caveats in concluding that the Milky Way bar is similar to that in model C10P06. First, as Obreja et al. (2022) suggested, a contracted NFW profile most likely describes the halo of the Milky Way, while our galaxy models adopt the Hernquist profile. Second, our models consider only isolated galaxies,

while non-axisymmetric perturbations by external triggers such as accretion and minor mergers with satellite galaxies can impact the bar evolution in real situations (Zana et al. 2018; Grand et al. 2019; Peschken & Lokas 2019; Ghosh et al. 2021; Cavanagh et al. 2022). The current halo spin of the Milky Way has likely been affected by the most recent major merger. Finally, while we adopt gas-free galaxy models, the presence of gas in the disk tends to reduce the bar slow-down rate (Seo et al. 2019; Beane et al. 2023). To understand the bar evolution of the Milky Way more accurately, it is desirable to run more realistic models by allowing for the halo density distribution, accretion, minor mergers, and the presence of gas and associated star formation.

6. CONCLUSIONS

We have presented the results of N -body simulations to investigate the effects of halo spin and the presence of a classical bulge on the bar formation and evolution. For this, we have borrowed two galaxy models from JK23 that have similar properties to the Milky Way: model C00 without a bulge and model C10 with a bulge whose mass is 10% of the disk mass. We have varied the spin parameter λ of the halo from 0.16 (prograde) to -0.16 (retrograde) in both series and run the models up to $t = 10$ Gyr. Our main conclusions are summarized below.

1. Simulations of the halo-only models show that our adopted halo is gravitationally stable if it does not rotate ($\lambda = 0$). When it rotates with $\lambda = \pm 0.16$, however, the halo itself is susceptible to forming $m = 2$ spirals via swing amplification, eventually growing into a weak bar. The spirals and bar rotate in the same sense as the halo spin, with a pattern speed of $\Omega_h \sim \pm 7 \text{ km s}^{-1} \text{ kpc}^{-1}$. This indicates that our rotating halo *alone* is vulnerable to the formation of non-axisymmetric structures rotating in the same direction as the halo.
2. The tendency of our spinning halo to form $m = 2$ non-axisymmetric structures even without external perturbations affects the bar growth time in an embedded disk. When $\lambda > 0$, $m = 2$ spirals growing via swing amplification in the disk interact constructively with the $m = 2$ mode in the prograde halo, promoting the bar formation in the inner disk. When λ is large, the spirals in the outer regions are strong enough to limit the further bar growth. When $\lambda < 0$, in contrast, the $m = 2$ mode in the disk interacts destructively with the $m = 2$ mode in the retrograde halo, delaying the bar formation. Since the outer disk is relatively less perturbed by the spirals, the bar in the disk

under a counter-rotating halo can grow stronger and longer than that in the models with large λ .

3. A bar grows by losing its angular momentum to both a halo and bulge, although the amount of angular momentum absorbed by the bulge is much less than that by the halo. The halo particles inside (outside) the corotation resonance R_{CR} with the bar can emit (absorb) angular momentum to (from) the bar. Since R_{CR} is larger for larger λ , the angular momentum transfer from disk to halo tends to be larger, causing the bar pattern speed Ω_b to decay faster, for smaller $\lambda > 0$. In models with $\lambda = 0.16$, the angular momentum absorption and emission are almost balanced, keeping Ω_b and bar strength nearly constant for a long period. Under a retrograde or non-spinning halo, in contrast, all the halo particles lag behind the bar and thus can absorb angular momentum from the bar efficiently. This causes Ω_b to decay relatively fast, almost independent of $\lambda \leq 0$.
4. All our models form a bar, and models with a strong bar develop a BPS bulge. In our models, the presence of a classical bulge reduces the bar growth and suppresses the buckling instability completely. In all models without a classical bulge (C00 series), a BPS bulge is produced rapidly through the buckling instability. In models with a classical bulge (C10 series), however, bars slowly thicken vertically via gravitational interactions with the disk particles.
5. In models with no classical bulge, the buckling instability tends to occur earlier along the sequence with smaller λ : a bar under a retrograde halo deforms earlier in the vertical direction than the prograde counterpart. For most of our models, the onset of the buckling instability corresponds to the ratio of the velocity dispersion $\sigma_z/\sigma_R \lesssim 0.47\text{--}0.60$ at $R = 2 \text{ kpc}$, roughly consistent with the previous results (e.g., Martinez-Valpuesta et al. 2006; Kwak et al. 2017), except model C00P16 which undergoes mild buckling instability even at $\sigma_z/\sigma_R \sim 0.75$. The models with a bulge have $\sigma_z/\sigma_R \gtrsim 0.55$ and remain stable to buckling instability.
6. Among our models, model C10P06 is similar to the Milky Way in terms of the halo spin and bar properties. It has the halo spin parameter of $\lambda = 0.06$, identical to the observationally inferred value (Obreja et al. 2022), and a classical bulge with mass 10% of the disk mass. The bar in this model has a semi-major axis of $R_b \sim 4\text{--}5 \text{ kpc}$ and

a pattern speed of $\Omega_b \sim 30\text{--}35 \text{ km s}^{-1} \text{ kpc}^{-1}$ for an extended period of time, which are consistent with the observed properties of the Milky Way bar.

ACKNOWLEDGMENTS

The work of D.J. was supported by Basic Science Research Program through the National Research Foundation of Korea (NRF) funded by the Ministry of Edu-

cation (RS-2023-00273275). The work of W.-T. K. was supported by a grant of the National Research Foundation of Korea (2022R1A2C1004810). Computational resources for this project were provided by the Supercomputing Center/Korea Institute of Science and Technology Information with supercomputing resources including technical support (KSC-2023-CRE-0175).

REFERENCES

- Aguerri, J. A. L., Méndez-Abreu, J., & Corsini, E. M. 2009, *A&A*, 495, 491, doi: [10.1051/0004-6361:200810931](https://doi.org/10.1051/0004-6361:200810931)
- Aguerri, J. A. L., Méndez-Abreu, J., Falcón-Barroso, J., et al. 2015, *A&A*, 576, A102, doi: [10.1051/0004-6361/201423383](https://doi.org/10.1051/0004-6361/201423383)
- Ansar, S., & Das, M. 2023, arXiv e-prints, arXiv:2311.11998, doi: [10.48550/arXiv.2311.11998](https://doi.org/10.48550/arXiv.2311.11998)
- Araki, S. 1987, *AJ*, 94, 99, doi: [10.1086/114451](https://doi.org/10.1086/114451)
- Athanassoula, E. 2002, *ApJL*, 569, L83, doi: [10.1086/340784](https://doi.org/10.1086/340784)
- . 2005, *MNRAS*, 358, 1477, doi: [10.1111/j.1365-2966.2005.08872.x](https://doi.org/10.1111/j.1365-2966.2005.08872.x)
- Beane, A., Hernquist, L., D’Onghia, E., et al. 2023, *ApJ*, 953, 173, doi: [10.3847/1538-4357/ace2b9](https://doi.org/10.3847/1538-4357/ace2b9)
- Bett, P., Eke, V., Frenk, C. S., et al. 2007, *MNRAS*, 376, 215, doi: [10.1111/j.1365-2966.2007.11432.x](https://doi.org/10.1111/j.1365-2966.2007.11432.x)
- Binney, J., & Tremaine, S. 2008, *Galactic Dynamics: Second Edition*
- Bland-Hawthorn, J., & Gerhard, O. 2016, *ARA&A*, 54, 529, doi: [10.1146/annurev-astro-081915-023441](https://doi.org/10.1146/annurev-astro-081915-023441)
- Bullock, J. S., Dekel, A., Kolatt, T. S., et al. 2001, *ApJ*, 555, 240, doi: [10.1086/321477](https://doi.org/10.1086/321477)
- Buta, R. J., Sheth, K., Athanassoula, E., et al. 2015, *ApJS*, 217, 32, doi: [10.1088/0067-0049/217/2/32](https://doi.org/10.1088/0067-0049/217/2/32)
- Cavanagh, M. K., Bekki, K., Groves, B. A., & Pfeffer, J. 2022, *MNRAS*, 510, 5164, doi: [10.1093/mnras/stab3786](https://doi.org/10.1093/mnras/stab3786)
- Chiba, R., & Kataria, S. K. 2024, *MNRAS*, 528, 4115, doi: [10.1093/mnras/stae288](https://doi.org/10.1093/mnras/stae288)
- Clarke, J. P., & Gerhard, O. 2022, *MNRAS*, 512, 2171, doi: [10.1093/mnras/stac603](https://doi.org/10.1093/mnras/stac603)
- Collier, A., & Madigan, A.-M. 2021, *ApJ*, 915, 23, doi: [10.3847/1538-4357/ac004d](https://doi.org/10.3847/1538-4357/ac004d)
- Collier, A., Shlosman, I., & Heller, C. 2018, *MNRAS*, 476, 1331, doi: [10.1093/mnras/sty270](https://doi.org/10.1093/mnras/sty270)
- . 2019a, *MNRAS*, 489, 3102, doi: [10.1093/mnras/stz2327](https://doi.org/10.1093/mnras/stz2327)
- . 2019b, *MNRAS*, 488, 5788, doi: [10.1093/mnras/stz2144](https://doi.org/10.1093/mnras/stz2144)
- Combes, F., Debbasch, F., Friedli, D., & Pfenniger, D. 1990, *A&A*, 233, 82
- Combes, F., & Sanders, R. H. 1981, *A&A*, 96, 164
- de Vaucouleurs, G. 1963, *ApJ*, 138, 934, doi: [10.1086/147696](https://doi.org/10.1086/147696)
- Debattista, V. P., Mayer, L., Carollo, C. M., et al. 2006, *ApJ*, 645, 209, doi: [10.1086/504147](https://doi.org/10.1086/504147)
- Debattista, V. P., & Sellwood, J. A. 2000, *ApJ*, 543, 704, doi: [10.1086/317148](https://doi.org/10.1086/317148)
- Di Matteo, P., Haywood, M., Combes, F., Semelin, B., & Snaith, O. N. 2013, *A&A*, 553, A102, doi: [10.1051/0004-6361/201220539](https://doi.org/10.1051/0004-6361/201220539)
- Díaz-García, S., Salo, H., Knapen, J. H., & Herrera-Endoqui, M. 2019, *A&A*, 631, A94, doi: [10.1051/0004-6361/201936000](https://doi.org/10.1051/0004-6361/201936000)
- Díaz-García, S., Salo, H., Laurikainen, E., & Herrera-Endoqui, M. 2016, *A&A*, 587, A160, doi: [10.1051/0004-6361/201526161](https://doi.org/10.1051/0004-6361/201526161)
- Dillamore, A. M., Belokurov, V., Evans, N. W., & Font, A. S. 2023, *MNRAS*, 519, L87, doi: [10.1093/mnras/519/l87](https://doi.org/10.1093/mnras/519/l87)
- Efstathiou, G., Lake, G., & Negroponte, J. 1982, *MNRAS*, 199, 1069, doi: [10.1093/mnras/199.4.1069](https://doi.org/10.1093/mnras/199.4.1069)
- Fall, S. M., & Efstathiou, G. 1980, *MNRAS*, 193, 189, doi: [10.1093/mnras/193.2.189](https://doi.org/10.1093/mnras/193.2.189)
- Fragkoudi, F., Di Matteo, P., Haywood, M., et al. 2017, *A&A*, 606, A47, doi: [10.1051/0004-6361/201630244](https://doi.org/10.1051/0004-6361/201630244)
- Frankel, N., Pillepich, A., Rix, H.-W., et al. 2022, *ApJ*, 940, 61, doi: [10.3847/1538-4357/ac9972](https://doi.org/10.3847/1538-4357/ac9972)
- Gadotti, D. A. 2011, *MNRAS*, 415, 3308, doi: [10.1111/j.1365-2966.2011.18945.x](https://doi.org/10.1111/j.1365-2966.2011.18945.x)
- Ghez, A. M., Salim, S., Weinberg, N. N., et al. 2008, *ApJ*, 689, 1044, doi: [10.1086/592738](https://doi.org/10.1086/592738)
- Ghosh, S., Saha, K., Di Matteo, P., & Combes, F. 2021, *MNRAS*, 502, 3085, doi: [10.1093/mnras/stab238](https://doi.org/10.1093/mnras/stab238)
- Gillessen, S., Eisenhauer, F., Fritz, T. K., et al. 2009a, *ApJL*, 707, L114, doi: [10.1088/0004-637X/707/2/L114](https://doi.org/10.1088/0004-637X/707/2/L114)
- Gillessen, S., Eisenhauer, F., Trippe, S., et al. 2009b, *ApJ*, 692, 1075, doi: [10.1088/0004-637X/692/2/1075](https://doi.org/10.1088/0004-637X/692/2/1075)
- Grand, R. J. J., van de Voort, F., Zjupa, J., et al. 2019, *MNRAS*, 490, 4786, doi: [10.1093/mnras/stz2928](https://doi.org/10.1093/mnras/stz2928)

- Halle, A., Di Matteo, P., Haywood, M., & Combes, F. 2018, *A&A*, 616, A86, doi: [10.1051/0004-6361/201832603](https://doi.org/10.1051/0004-6361/201832603)
- Helmi, A. 2020, *ARA&A*, 58, 205, doi: [10.1146/annurev-astro-032620-021917](https://doi.org/10.1146/annurev-astro-032620-021917)
- Hernquist, L. 1990, *ApJ*, 356, 359, doi: [10.1086/168845](https://doi.org/10.1086/168845)
- Hetznecker, H., & Burkert, A. 2006, *MNRAS*, 370, 1905, doi: [10.1111/j.1365-2966.2006.10616.x](https://doi.org/10.1111/j.1365-2966.2006.10616.x)
- Hohl, F. 1976, *AJ*, 81, 30, doi: [10.1086/111849](https://doi.org/10.1086/111849)
- Hoyle, F. 1951, in *Problems of Cosmical Aerodynamics*, 195
- Iannuzzi, F., & Athanassoula, E. 2015, *MNRAS*, 450, 2514, doi: [10.1093/mnras/stv764](https://doi.org/10.1093/mnras/stv764)
- Iles, E. J., Pettitt, A. R., Okamoto, T., & Kawata, D. 2024, *MNRAS*, 527, 2799, doi: [10.1093/mnras/stad3377](https://doi.org/10.1093/mnras/stad3377)
- Jang, D., & Kim, W.-T. 2023, *ApJ*, 942, 106, doi: [10.3847/1538-4357/aca7bc](https://doi.org/10.3847/1538-4357/aca7bc)
- Jiang, F., Dekel, A., Kneller, O., et al. 2019, *MNRAS*, 488, 4801, doi: [10.1093/mnras/stz1952](https://doi.org/10.1093/mnras/stz1952)
- Kataria, S. K., & Das, M. 2018, *MNRAS*, 475, 1653, doi: [10.1093/mnras/stx3279](https://doi.org/10.1093/mnras/stx3279)
- Kataria, S. K., & Shen, J. 2022, *ApJ*, 940, 175, doi: [10.3847/1538-4357/ac9df1](https://doi.org/10.3847/1538-4357/ac9df1)
- Kawata, D., Grand, R. J. J., Gibson, B. K., et al. 2017, *MNRAS*, 464, 702, doi: [10.1093/mnras/stw2363](https://doi.org/10.1093/mnras/stw2363)
- Kwak, S., Kim, W.-T., Rey, S.-C., & Kim, S. 2017, *ApJ*, 839, 24, doi: [10.3847/1538-4357/aa674c](https://doi.org/10.3847/1538-4357/aa674c)
- Kwak, S., Kim, W.-T., Rey, S.-C., & Quinn, T. R. 2019, *ApJ*, 887, 139, doi: [10.3847/1538-4357/ab5716](https://doi.org/10.3847/1538-4357/ab5716)
- Laurikainen, E., Salo, H., & Buta, R. 2004, *ApJ*, 607, 103, doi: [10.1086/383462](https://doi.org/10.1086/383462)
- Lee, Y. H., Park, M.-G., Hwang, H. S., et al. 2022, *ApJ*, 926, 58, doi: [10.3847/1538-4357/ac3bc1](https://doi.org/10.3847/1538-4357/ac3bc1)
- Li, X., Shlosman, I., Pfenniger, D., & Heller, C. 2023, *MNRAS*, 520, 1243, doi: [10.1093/mnras/stad076](https://doi.org/10.1093/mnras/stad076)
- . 2024, *MNRAS*, 527, 11026, doi: [10.1093/mnras/stad3907](https://doi.org/10.1093/mnras/stad3907)
- Lieb, E., Collier, A., & Madigan, A.-M. 2022, *MNRAS*, 509, 685, doi: [10.1093/mnras/stab2904](https://doi.org/10.1093/mnras/stab2904)
- Lokas, E. L. 2019, *A&A*, 629, A52, doi: [10.1051/0004-6361/201936056](https://doi.org/10.1051/0004-6361/201936056)
- Long, S., Shlosman, I., & Heller, C. 2014, *ApJL*, 783, L18, doi: [10.1088/2041-8205/783/1/L18](https://doi.org/10.1088/2041-8205/783/1/L18)
- Lynden-Bell, D. 1960, *MNRAS*, 120, 204, doi: [10.1093/mnras/120.3.204](https://doi.org/10.1093/mnras/120.3.204)
- Marinova, I., & Jogee, S. 2007, *ApJ*, 659, 1176, doi: [10.1086/512355](https://doi.org/10.1086/512355)
- Martinez-Valpuesta, I., Shlosman, I., & Heller, C. 2006, *ApJ*, 637, 214, doi: [10.1086/498338](https://doi.org/10.1086/498338)
- Méndez-Abreu, J., Sánchez-Janssen, R., Aguerri, J. A. L., Corsini, E. M., & Zarattini, S. 2012, *ApJL*, 761, L6, doi: [10.1088/2041-8205/761/1/L6](https://doi.org/10.1088/2041-8205/761/1/L6)
- Menéndez-Delmestre, K., Sheth, K., Schinnerer, E., Jarrett, T. H., & Scoville, N. Z. 2007, *ApJ*, 657, 790, doi: [10.1086/511025](https://doi.org/10.1086/511025)
- Merritt, D., & Sellwood, J. A. 1994, *ApJ*, 425, 551, doi: [10.1086/174005](https://doi.org/10.1086/174005)
- Navarro, J. F., Frenk, C. S., & White, S. D. M. 1996, *ApJ*, 462, 563, doi: [10.1086/177173](https://doi.org/10.1086/177173)
- Obreja, A., Buck, T., & Macciò, A. V. 2022, *A&A*, 657, A15, doi: [10.1051/0004-6361/202140983](https://doi.org/10.1051/0004-6361/202140983)
- Oh, S. H., Kim, W.-T., Lee, H. M., & Kim, J. 2008, *ApJ*, 683, 94, doi: [10.1086/588184](https://doi.org/10.1086/588184)
- Ostriker, J. P., & Peebles, P. J. E. 1973, *ApJ*, 186, 467, doi: [10.1086/152513](https://doi.org/10.1086/152513)
- Patsis, P. A., Skokos, C., & Athanassoula, E. 2002, *MNRAS*, 337, 578, doi: [10.1046/j.1365-8711.2002.05943.x](https://doi.org/10.1046/j.1365-8711.2002.05943.x)
- Peebles, P. J. E. 1969, *ApJ*, 155, 393, doi: [10.1086/149876](https://doi.org/10.1086/149876)
- . 1971, *A&A*, 11, 377
- Peschken, N., & Lokas, E. L. 2019, *MNRAS*, 483, 2721, doi: [10.1093/mnras/sty3277](https://doi.org/10.1093/mnras/sty3277)
- Petersen, M. S., Weinberg, M. D., & Katz, N. 2016, *MNRAS*, 463, 1952, doi: [10.1093/mnras/stw2141](https://doi.org/10.1093/mnras/stw2141)
- Pfenniger, D., & Friedli, D. 1991, *A&A*, 252, 75
- Portail, M., Wegg, C., Gerhard, O., & Ness, M. 2017, *MNRAS*, 470, 1233, doi: [10.1093/mnras/stx1293](https://doi.org/10.1093/mnras/stx1293)
- Raha, N., Sellwood, J. A., James, R. A., & Kahn, F. D. 1991, *Nature*, 352, 411, doi: [10.1038/352411a0](https://doi.org/10.1038/352411a0)
- Roshan, M., Ghafourian, N., Kashfi, T., et al. 2021, *MNRAS*, 508, 926, doi: [10.1093/mnras/stab2553](https://doi.org/10.1093/mnras/stab2553)
- Saha, K., & Elmegreen, B. 2018, *ApJ*, 858, 24, doi: [10.3847/1538-4357/aabacd](https://doi.org/10.3847/1538-4357/aabacd)
- Saha, K., & Naab, T. 2013, *MNRAS*, 434, 1287, doi: [10.1093/mnras/stt1088](https://doi.org/10.1093/mnras/stt1088)
- Sellwood, J. A. 1980, *A&A*, 89, 296
- Sellwood, J. A., & Athanassoula, E. 1986, *MNRAS*, 221, 195, doi: [10.1093/mnras/221.2.195](https://doi.org/10.1093/mnras/221.2.195)
- Sellwood, J. A., & Carlberg, R. G. 1984, *ApJ*, 282, 61, doi: [10.1086/162176](https://doi.org/10.1086/162176)
- Sellwood, J. A., & Gerhard, O. 2020, *MNRAS*, 495, 3175, doi: [10.1093/mnras/staa1336](https://doi.org/10.1093/mnras/staa1336)
- Seo, W.-Y., Kim, W.-T., Kwak, S., et al. 2019, *ApJ*, 872, 5, doi: [10.3847/1538-4357/aafc5f](https://doi.org/10.3847/1538-4357/aafc5f)
- Shen, J., Rich, R. M., Kormendy, J., et al. 2010, *ApJL*, 720, L72, doi: [10.1088/2041-8205/720/1/L72](https://doi.org/10.1088/2041-8205/720/1/L72)
- Smirnov, A. A., & Sotnikova, N. Y. 2018, *MNRAS*, 481, 4058, doi: [10.1093/mnras/sty2423](https://doi.org/10.1093/mnras/sty2423)
- Sormani, M. C., Binney, J., & Magorrian, J. 2015, *MNRAS*, 454, 1818, doi: [10.1093/mnras/stv2067](https://doi.org/10.1093/mnras/stv2067)
- Springel, V., Pakmor, R., Zier, O., & Reinecke, M. 2021, *MNRAS*, 506, 2871, doi: [10.1093/mnras/stab1855](https://doi.org/10.1093/mnras/stab1855)

- Toomre, A. 1966, in Geophysical Fluid Dynamics Ref. No. 66-46, ed. W. V. R. Malkus, (Woods Hole, MA: Woods Hole Oceanographic Institute), 111
- Toomre, A. 1981, in Structure and Evolution of Normal Galaxies, ed. S. M. Fall & D. Lynden-Bell, 111–136
- Villa-Vargas, J., Shlosman, I., & Heller, C. 2009, *ApJ*, 707, 218, doi: [10.1088/0004-637X/707/1/218](https://doi.org/10.1088/0004-637X/707/1/218)
- Vitvitska, M., Klypin, A. A., Kravtsov, A. V., et al. 2002, *ApJ*, 581, 799, doi: [10.1086/344361](https://doi.org/10.1086/344361)
- Wegg, C., Gerhard, O., & Portail, M. 2015, *MNRAS*, 450, 4050, doi: [10.1093/mnras/stv745](https://doi.org/10.1093/mnras/stv745)
- Weinberg, M. D. 1985, *MNRAS*, 213, 451, doi: [10.1093/mnras/213.3.451](https://doi.org/10.1093/mnras/213.3.451)
- White, S. D. M. 1984, *ApJ*, 286, 38, doi: [10.1086/162573](https://doi.org/10.1086/162573)
- Whyte, L. F., Abraham, R. G., Merrifield, M. R., et al. 2002, *MNRAS*, 336, 1281, doi: [10.1046/j.1365-8711.2002.05879.x](https://doi.org/10.1046/j.1365-8711.2002.05879.x)
- Xiang, K. M., Nataf, D. M., Athanassoula, E., et al. 2021, *ApJ*, 909, 125, doi: [10.3847/1538-4357/abdab5](https://doi.org/10.3847/1538-4357/abdab5)
- Yurin, D., & Springel, V. 2014, *MNRAS*, 444, 62, doi: [10.1093/mnras/stu1421](https://doi.org/10.1093/mnras/stu1421)
- Zana, T., Dotti, M., Capelo, P. R., et al. 2018, *MNRAS*, 473, 2608, doi: [10.1093/mnras/stx2503](https://doi.org/10.1093/mnras/stx2503)